

An Eco-friendly Soft Template Synthesis of Mesostructured Silica-Carbon Nanocomposites for Acid Catalysis

Ruyi Zhong,^[a] Li Peng,^{*[a]} Filip de Clippel,^[a] Cedric Gommès,^[b] Bart Goderis,^[c] Xiaoxing Ke,^[d] Gustaaf Van Tendeloo,^[d] Pierre A. Jacobs,^[a] and Bert F. Sels^{*[a]}

The synthesis of ordered mesoporous silica-carbon composites was explored by employing TEOS and sucrose as the silica and carbon precursor respectively, and the triblock copolymer F127 as a structure-directing agent via an evaporation-induced self-assembly (EISA) process. It is demonstrated that the synthesis procedures allow for control of the textural properties and final composition of these silica-carbon nanocomposites via adjustment of the effective SiO₂/C weight ratio. Characterization by SAXS, N₂ physisorption, HRTEM, TGA, and ¹³C and ²⁹Si solid-state MAS NMR show a 2D hexagonal mesostructure with uniform large pore size ranging from 5.2 to 7.6 nm, comprising

of separate carbon phases in a continuous silica phase. Ordered mesoporous silica and non-ordered porous carbon can be obtained by combustion of the pyrolyzed nanocomposites in air or etching with HF solution, respectively. Sulfonic acid groups can be readily introduced to such kind of silica-carbon nanocomposites by a standard sulfonation procedure with concentrated sulfuric acid. Excellent acid-catalytic activities and selectivities for the dimerization of styrene to produce 1,3-diphenyl-1-butene and dimerization of α -methylstyrene to unsaturated dimers were demonstrated with the sulfonated materials.

Introduction

Since the discovery of ordered mesoporous silica materials in 1990s, synthesis and applications of mesoporous solids have received intensive attention, owing to their wide applications in catalysis, adsorption, separation, devices, and drug delivery, etc.^[1–7] With well-developed soft-template and hard-template (nanocasting) methods, mesoporous materials based on various compositions have been prepared, such as silica, heteroatom doped silica, organosilica, metal oxide, metal, polymer, carbon as well as composite.^[8–12] Among these materials, mesoporous silica-carbon composites are an attractive family of

novel mesoporous materials. Besides their well-controlled pore structures, high surface areas, and large and tunable pore sizes which facilitate the diffusion of reactants and products inside the pores, they combine the properties of inorganic components, such as good mechanical and thermal stability, as well as organic components, such as hydrophobicity and versatility for further functionalization.^[1] These materials have, consequently, received significant attention recently for their potential applications in catalysis, adsorption, separation, optics devices, and electrodes.^[13–23] Ordered mesoporous silica-carbon composites prepared by infiltration of carbon precursors into preformed mesoporous silica followed by carbonization.^[14–20] However, this procedure is laborious and time consuming, owing to the involvement of the pre-formation of the ordered mesoporous silica template. Mesoporous silica-carbon composites can also be prepared by carbonization of mesoporous organosilica/surfactant mesophases, or mesoporous silica/surfactant mesophases.^[24–28] One drawback is that organosilanes are expensive and difficult to obtain and another drawback is that organic functional groups or surfactant may block the pores. Recently, a multi-component assembly approach has been used to prepare ordered mesoporous silica-carbon nanocomposites by using phenolic resins (resols) as carbon precursor, TEOS as silica precursor, and triblock copolymer F127 as a template.^[29,30] The successful synthesis is mainly attributed to the unique characteristics of the thermosetting phenolic resins for the formation of three-dimensional (3D) cross-linked networks, such as abundant benzyl and phenolic hydroxyl groups, and controllable polymerization rate.^[31] However, resols are hazardous as they consist of derivatives of phenols and formaldehyde which are all carcinogenic. Therefore, it is interesting to devel-

[a] R. Zhong, L. Peng, F. de Clippel, P. A. Jacobs, B. F. Sels
Centre for Surface Science and Catalysis
KU Leuven
Kasteelpark Arenberg 23 - bus 2461, 3001 Heverlee (Belgium)
Fax: (+32)016-321998
E-mail: lisa.lipeng@gmail.com
bert.sels@biw.kuleuven.be

[b] C. Gommès
Department of Chemical Engineering
University of Liege
Building B6A, 4000 Liege (Belgium)

[c] B. Goderis
Polymer Chemistry and Materials
KU Leuven
Celestijnenlaan 200f - bus 2404, 3001 Heverlee (Belgium)

[d] X. Ke, G. V. Tendeloo
Electron Microscopy for Materials Science
Universiteit Antwerpen
Groenenborgerlaan 171, 2020 Antwerpen (Belgium)

Supporting information for this article is available on the WWW under <http://dx.doi.org/10.1002/cctc.201500728>.

This publication is part of a Special Issue on "Carbon in the Catalysis Community". Once the full issue has been assembled, a link to its Table of Contents will appear here.

op a novel and eco-friendly carbon precursor which can replace resols in the synthesis.

Here we explore the synthesis of novel ordered mesoporous silica-carbon nanocomposite using a simple and efficient synthesis through multi-component assembly by using TEOS, sucrose as precursors and F127 as a template. Sucrose was chosen as the carbon precursor given following considerations. Firstly, sucrose is a readily-available natural product, which will make this process easy and green. Secondly, the multiple adjacent hydroxyl groups of sucrose probably promote the formation of hydrogen bonding with the polar PEO blocks of F127 and silica oligomers, which makes the tri-constituent co-assembly possible. Thirdly, sulfonic acid groups (SO_3H) can be readily introduced to incompletely carbonized sucrose³² which gives rise to potential application of such silica-carbon nanocomposites as solid-acid catalysts.

Sucrose has been widely used as carbon precursor for the synthesis of mesoporous carbon through a hard-template method.^[33,34] However, to the authors' knowledge, sucrose has seldom been used as carbon precursor for the direct soft-template synthesis of ordered mesoporous structure. Herein, evaporation-induced co-assembly of TEOS, sucrose and F127 for the synthesis of mesoporous silica-carbon nanocomposites was extensively investigated. These nanocomposites possess an ordered 2D hexagonal mesostructure, high surface areas ($120\text{--}500\text{ m}^2\text{g}^{-1}$), and uniform large pore sizes ($5.2\text{--}7.6\text{ nm}$). The textural properties and compositions can be easily tuned by adjusting the initial mass ratios of TEOS to sucrose and the pyrolysis temperature, which were further demonstrated to greatly influence the catalytic performance. The sulfonated silica-carbon nanocomposites were applied to the dimerization of styrene to produce linear unsaturated dimer, 1,3-diphenyl-1-butene (DPB) and the dimerization of α -methylstyrene (AMS) to produce acyclic dimers. These unsaturated dimers are industrially important as chain transfer agents. Moreover, the carbon-bound sulfonic acid groups will show high accessibility to such hydrophobic substrate molecules due to the apolar nature of the carbon component and the mesoporosity of the nanocomposite.

Results and Discussion

Synthesis of ordered mesoporous silica-carbon composites

Mesoporous silica-carbon nanocomposites are prepared from an EISA method by using triblock copolymer F127 ($\text{EO}_{106}\text{PO}_{70}\text{EO}_{106}$) as a template, ethanol and H_2O as solvent, TEOS and sucrose as silica and carbon precursors, respectively.^[35] By adjusting the initial mass ratios of TEOS and sucrose, $\text{Si}_{33}\text{C}_{66}$, $\text{Si}_{50}\text{C}_{50}$, and $\text{Si}_{66}\text{C}_{33}$ nanocomposites with different silica and carbon content can be obtained. All these as-synthesized samples from EISA processes are light yellow to deep yellow membranes without obvious macrophase separation. SAXS patterns of the as-synthesized silica-carbon nanocomposites

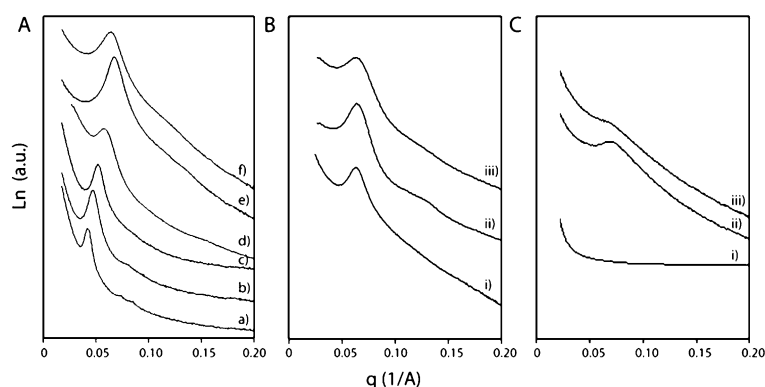


Figure 1. SAXS patterns of: A) silica-carbon nanocomposites samples before a) $\text{Si}_{33}\text{C}_{66}$, b) $\text{Si}_{50}\text{C}_{50}$, c) $\text{Si}_{66}\text{C}_{33}$, and after pyrolysis d) $\text{Si}_{33}\text{C}_{66}\text{-1073}$, e) $\text{Si}_{50}\text{C}_{50}\text{-1073}$, f) $\text{Si}_{66}\text{C}_{33}\text{-1073}$; and after removal of carbon or silica from the pyrolyzed composites to obtain pure B) silica or C) carbon samples, i), ii), and iii) corresponding to their mother composites of $\text{Si}_{33}\text{C}_{66}$, $\text{Si}_{50}\text{C}_{50}$, and $\text{Si}_{66}\text{C}_{33}$, respectively.

(Figure 1A, a–c) exhibit a main scattering peak at a vector of q^* and other dim peaks for some samples at larger vectors. These dim peaks are located at vectors of $\sqrt{3}/2 q^*$ and $2q^*$, and characteristic of an ordered 2D hexagonal mesostructure with the $p6mm$ symmetry. The ordered domains are of a relatively limited size, which in turn causes the blurriness of the secondary scattering peaks due to the Scherrer line broadening effect. The average distance between neighboring pores was calculated by using the formula $a = 4\pi/(\sqrt{3} q^*)$, and listed in Table 1.

After pyrolysis under N_2 at 1073 K, the silica-carbon nanocomposites show SAXS scattering peaks (Figure 1A, d–f), assigned to the (100) reflection of the hexagonal $p6mm$ mesostructure. The pore distance was shortened compared to the parent silica-carbon nanocomposite, owing to the transformation of sucrose into carbonization products and the decomposition of the template F127. The shrinkage degree decreased with the increasing silica/carbon ratio, which demonstrates the stabilization effect of the silica component for the whole mesostructure during thermal treatment. The final pore distance of $\text{Si}_{33}\text{C}_{66}\text{-1073}$ was 12.4 nm, slightly larger than $\text{Si}_{50}\text{C}_{50}\text{-1073}$ (11.3 nm) and $\text{Si}_{66}\text{C}_{33}\text{-1073}$ (11.5 nm). Furthermore, the scattering peak of $\text{Si}_{33}\text{C}_{66}\text{-1073}$ was much weaker than that of $\text{Si}_{50}\text{C}_{50}\text{-1073}$ and $\text{Si}_{66}\text{C}_{33}\text{-1073}$, and the reduced contrast may be attributable to the filling of mesopores by carbon. Typical TEM images of silica-carbon nanocomposite and its derived pure silica and carbon materials, $\text{Si}_{50}\text{C}_{50}\text{-1073}$, $\text{Si}_{50}\text{C}_{50}\text{-Si}$ and $\text{Si}_{50}\text{C}_{50}\text{-C}$ are shown in Figure 2.

Uniform hexagonally arranged channel arrays are observed in large domains in $\text{Si}_{50}\text{C}_{50}\text{-1073}$ (Figure 2A), clearly showing a highly ordered hexagonal mesostructure. The average distance between neighboring pores determined from the TEM image was 10.9 nm, consistent with the value of 11.3 nm from its SAXS pattern. The average pore size was 6.0 nm and the pore-wall thickness was 5.3 nm for $\text{Si}_{50}\text{C}_{50}\text{-1073}$ according to its TEM image.

N_2 sorption isotherms and pore size distributions of $\text{Si}_m\text{C}_n\text{-1073}$ nanocomposites are shown in Figure 3A. The corre-

Table 1. Composite and physicochemical properties of carbon/silica nanocomposites and of the corresponding silica and carbon frameworks obtained after the removal of carbon and silica, respectively.^[a]

Sample	C [%]	<i>a</i> [nm]	<i>S</i> _{BET} [m ² g ⁻¹]	<i>V</i> _{tot} [cm ³ g ⁻¹]	<i>V</i> _{meso} [cm ³ g ⁻¹]	<i>V</i> _{micro} [cm ³ g ⁻¹]	<i>D</i> [nm]
Si ₃₃ C ₆₆	–	16.8	–	–	–	–	–
Si ₅₀ C ₅₀	–	15.3	–	–	–	–	–
Si ₆₆ C ₃₃	–	13.9	–	–	–	–	–
Si ₃₃ C ₆₆ -1073	49	12.4	155	0.06	0.01	0.05	5.2
Si ₅₀ C ₅₀ -1073	32	11.3	177	0.20	0.16	0.04	6.3
Si ₆₆ C ₃₃ -1073	19	11.5	156	0.22	0.20	0.02	6.4
Si ₃₃ C ₆₆ -Si	0	11.7	188	0.12	0.12	0.0	2.6, 5.0
Si ₅₀ C ₅₀ -Si	0	10.6	410	0.36	0.33	0.03	2.6, 6.2
Si ₆₆ C ₃₃ -Si	0	11.4	381	0.41	0.38	0.03	2.6, 6.2
Si ₃₃ C ₆₆ -C	100	–	794	0.39	0.15	0.04	–
Si ₅₀ C ₅₀ -C	100	10.5	1118	0.82	0.75	0.07	3.5
Si ₆₆ C ₃₃ -C	100	–	1086	0.69	0.59	0.10	2.6
Si ₃₃ C ₆₆ -673-SO ₃ H	62	13.6	471	0.20	0.02	0.18	–
Si ₅₀ C ₅₀ -673-SO ₃ H	49	12.7	424	0.25	0.13	0.12	7.6
Si ₆₆ C ₃₃ -673-SO ₃ H	30	12.7	493	0.44	0.33	0.11	6.9
Si ₃₃ C ₆₆ -823-SO ₃ H	54	12.8	–	–	–	–	–
Si ₅₀ C ₅₀ -823-SO ₃ H	38	11.9	124	0.10	0.07	0.03	6.9
Si ₆₆ C ₃₃ -823-SO ₃ H	23	11.9	332	0.39	0.35	0.04	6.7

[a] C% were the mass percentage of carbon in the dry samples, determined from TGA; Surface area (*S*_{BET}) is calculated by the BET method; Total pore volume (*V*_{tot}) was calculated from the saturation plateau at high relative pressures; Mesopore volume (*V*_{meso}) was calculated after subtraction of the micropore volume (*V*_{micro}) as obtained by the *t*-plot method; Pore size (*D*) at the maxima of pore size distribution was calculated from adsorption branches of the isotherms, based on the BJH model.

sponding values of BET surface area, total pore volume, mesopore volume and average mesopore size are presented in Table 1. Si₅₀C₅₀-1073 and Si₆₆C₃₃-1073 show a type IV curve with a H₁-type hysteresis loop, typical of a well-ordered cylindrical mesoporous structure. Their isotherms show distinct steep capillary condensation steps at *P/P*₀ = 0.60–0.75, corresponding to uniform mesopores. The pore size of Si₅₀C₅₀-1073 was 6.3 nm with a narrow distribution and the pore-wall thickness was 5.0 nm, which is coincident with the TEM measurement. The mesopore volumes of Si₅₀C₅₀-1073 and Si₆₆C₃₃-1073 were 0.20 and 0.22 cm³g⁻¹ respectively, predominant in the total porosity. These silica-carbon nanocomposites mainly contain 5.5–7.5 nm mesopores with silica and carbon components coexisting in the pore-walls, whereas the carbon-rich Si₃₃C₆₆-1073 shows a type IV isotherms with a H₁ + H₃ mixed hysteresis loop. The total pore volume was only 0.06 cm³g⁻¹ and the mesoporosity was hardly present (*V*_{meso} = 0.01 cm³g⁻¹). However, the SAXS pattern of Si₃₃C₆₆-1073 (Figure 1A, a) reveals its hexagonal mesostructure. As determined from the TGA analysis (Figure S1), carbon content in Si₃₃C₆₆-1073 was 49%, a lot higher than in Si₅₀C₅₀-1073 (32%) and Si₆₆C₃₃-1073 (19%). It is, therefore, very likely that excessive part of the carbon phase in Si₃₃C₆₆-1073 located inside the silica-carbon mesopores and caused the closure of most mesopores. The carbon in the mesopores was probably in the form of aggregates of small platy carbon sheets, forming slit-shaped pores, causing the H₃-type hysteresis loop.

Pure silica and carbon materials from silica-carbon composites

Mesoporous silica materials were obtained from the silica-carbon nanocomposites after calcination in air to remove the carbon component. The SAXS patterns of pure silica materials (Figure 1B) show one scattering peak which is assigned to a hexagonally ordered mesostructure. The calculated average distances between neighboring pores, listed in Table 1, are close to the values of their parent nanocomposites. Therefore, the framework of silica was almost kept intact during the calcination process and was always of *p6mm* symmetry, despite the difference in carbon content between the nanocomposites. The TEM image of Si₅₀C₅₀-Si (Figure 2B) resembles well that of Si₅₀C₅₀-1073, which implies that the carbon phase is dispersed homogeneously in the silica framework.

N₂ sorption isotherms of Si₅₀C₅₀-Si and Si₆₆C₃₃-Si (Figure 3B, up) are type IV curves with a H₂-type hysteresis loop. The steep capillary condensation also mainly occurred at a relative pressure range of 0.60–0.75, corresponding to uniform mesopores of 5.5–7.5 nm similar to those in their parent silica-carbon nanocomposites. Combined with the SAXS results, these mesopores originate from the F127 micell organization in the original structure and are opened by thermally decomposing the F127 molecules. However, the hysteresis loops of pure silica materials were partially deformed, with regard to the ideal parallel H₁-type loops of their parent silica-carbon nanocomposites, probably due to the presence of secondary mesopores, which was generated during the burn-off of carbon in the pore-walls. The pore size distributions of Si₅₀C₅₀-Si and Si₆₆C₃₃-Si (Figure 3B, bottom) were indeed bimodal, showing pore sizes centered at 2.6 nm in addition to the primary pore size of 6.2 nm. These results indicate that the carbon phase in Si₅₀C₅₀-1073 and Si₆₆C₃₃-1073 is located in small domains of mean size of 2.6 nm in the pore-walls.

N₂ sorption isotherm of Si₃₃C₆₆-Si (Figure 3B, up) is type IV curve with a H₂-type hysteresis loop, significantly different from its parent Si₃₃C₆₆-1073. The opening of mesopores which were previously filled by amorphous carbon, accounts for the large H₂-type hysteresis loop observed on the pure silica material and the simultaneously elimination of the H₃-type loop of the intrapore carbon sheets. Bimodal pore sizes are also observed for the Si₃₃C₆₆-Si (Figure 3B, bottom). The smaller mesopores were ≈ 2.6 nm, the same as Si₅₀C₅₀-Si and Si₆₆C₃₃-Si, which indicates similar nanosized carbon domains located inside the composite pore-walls of Si₃₃C₆₆-1073. The BET surface area, the total porosity and the mesoporosity of these three pure silica materials all increased compared to their parent silica-carbon nanocomposites (Table 1, entries 4–9), also evidencing that the carbon component forms small carbon sheets and is dispersed within the pore-walls in the nanocomposites. After removal of carbon component, mesoporous silica

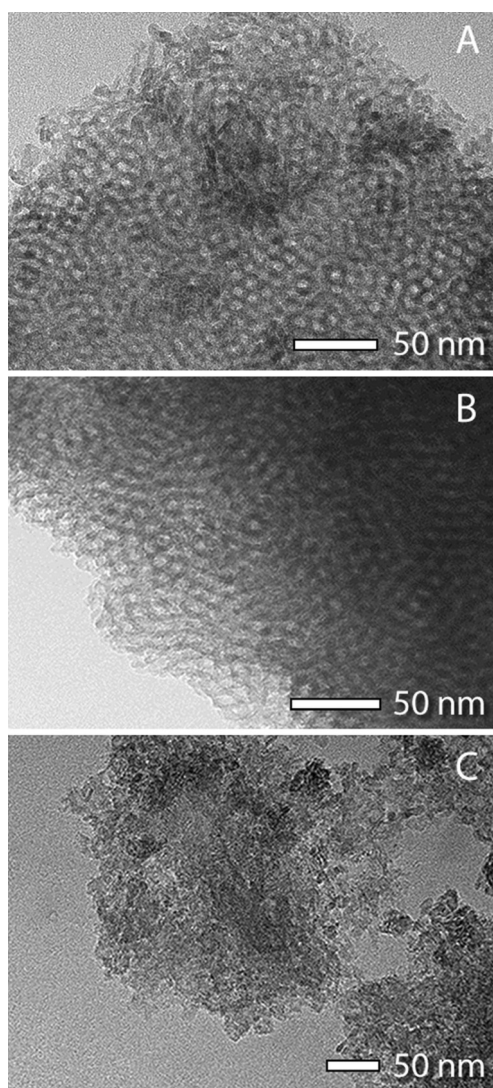


Figure 2. TEM images of the A) silica-carbon nanocomposite $\text{Si}_{50}\text{C}_{50}$ -1073 and the pure B) silica ($\text{Si}_{50}\text{C}_{50}$ -Si), and C) carbon ($\text{Si}_{50}\text{C}_{50}$ -C) samples derived therefrom after removal of carbon and silica, respectively.

materials can be obtained with a hierarchical organization of the pore architecture.

Pure carbon materials were obtained from the silica-carbon nanocomposites by etching of silica component with HF solution. SAXS patterns for these Si_mC_n -C materials are shown in Figure 1C. Without the presence of silica component, the ordering of the mesostructure was largely impaired. $\text{Si}_{50}\text{C}_{50}$ -C displayed a weak and broad scattering peak, and the scattering peak of $\text{Si}_{66}\text{C}_{33}$ -C was even more obscure. However, the calculated average pore distances for both $\text{Si}_{50}\text{C}_{50}$ -C and $\text{Si}_{66}\text{C}_{33}$ -C was not far from the values for their parent silica-carbon nanocomposites, showing the traces of the original hexagonal mesostructure. The severe degradation of the mesostructure after silica removal in the composite pore-walls is also revealed by the TEM image of $\text{Si}_{50}\text{C}_{50}$ -C (Figure 2C). As for $\text{Si}_{33}\text{C}_{66}$ -C, no scattering peak at all was observed from its SAXS pattern. This irregular porous $\text{Si}_{33}\text{C}_{66}$ -C material could be constructed by the small carbon sheets from the composite pore-walls and those

amorphous carbon inside the F127-derived big mesopores. These results show that carbon is not well organized in a continuous phase throughout the materials, when compared to silica, leading to a loss of pore structure upon removal of silica.

N_2 sorption isotherms of all these three derivative carbon materials (Figure 3C, top) are of type-IV with a $\text{H}_2 + \text{H}_3$ -type hysteresis loop, consistent with a disordered pore structure. Etching of silica component would result in lots of voids in the pore-walls and largely reduce the mesoscopic regularity. These small mesopores resulted from silica removal coincided well with the left-shifted capillary condensation steps in a relative pressure range of 0.45–0.65, in relative to the parent silica-carbon nanocomposites. Meanwhile, the BET surface area ($794\text{--}1118\text{ m}^2\text{g}^{-1}$) and mesopore volume ($0.15\text{--}0.75\text{ cm}^3\text{g}^{-1}$) (Table 1) were increased after removal of silica component, also due to the newly generated small mesopores (Figure 3C, bottom) in the pore-walls. The mesoporosity of $\text{Si}_{33}\text{C}_{66}$ -C was still much smaller than $\text{Si}_{50}\text{C}_{50}$ -C and $\text{Si}_{66}\text{C}_{33}$ -C as a result of the microporous carbon aggregates in the F127-derived large mesopores in $\text{Si}_{33}\text{C}_{66}$ -1073.

Formation of mesostructured silica-carbon framework

We propose that the formation of composites undergoes a tri-constituent assembly process of organic sucrose precursor, silicate oligomer generated through the hydrolysis of TEOS, and amphiphilic triblock copolymer F127 (Scheme 1). F127, sucrose and TEOS are well dissolved in acidic EtOH/ H_2O solution. TEOS is hydrolyzed rapidly in presence of HCl to form silicate oligomers. With the evaporation of EtOH solvent at 313 K, the triblock copolymer F127 tends to aggregate into columnar micelles with hydrophobic PPO block as a core surrounded by a polar PEO block shell. Simultaneously, sucrose and the silicate oligomers, both possessing plenty of hydroxyl groups, interact strongly with the long EO chains of the copolymer via hydrogen-bonding. Sucrose and the silicate oligomers are thus aggregated around the EO domains of the F127 micelles. Meanwhile, under acidic conditions, PEO blocks, as well as OH groups of silica oligomers and sucrose, can be partially protonated and can self-assemble together through the electrostatic interaction with Cl^- anions.^[36] By the two assembly mechanisms, continuous evaporation of ethanol promotes the construction of hexagonally mesostructured composites (Scheme 1A) of F127 micelles with sucrose and silicate oligomers. The condensation and cross-linking of the silicate oligomers to form SiO_2 framework proceeds simultaneously, whereas sucrose does not polymerize at 313 K. Owing to the tetrahedral structure of SiO_2 , cross-linking of silicate oligomers can occur around sucrose molecules and incorporate these “carbon domains” into the SiO_2 framework.^[29] This can also be understood from the point that silica oligomers self-assemble around the secondary non-surfactant template, sucrose,^[37] in the hydrophilic polyethylene oxide (PEO) region of the F127 micelles.

When sucrose is added to a high amount, like in the case of $\text{Si}_{33}\text{C}_{66}$ (F127/TEOS/sucrose = 1:1.3:1.74 in mass ratio), in contrast with $\text{Si}_{50}\text{C}_{50}$ (F127/TEOS/sucrose = 1:1.3:0.87 in mass ratio)

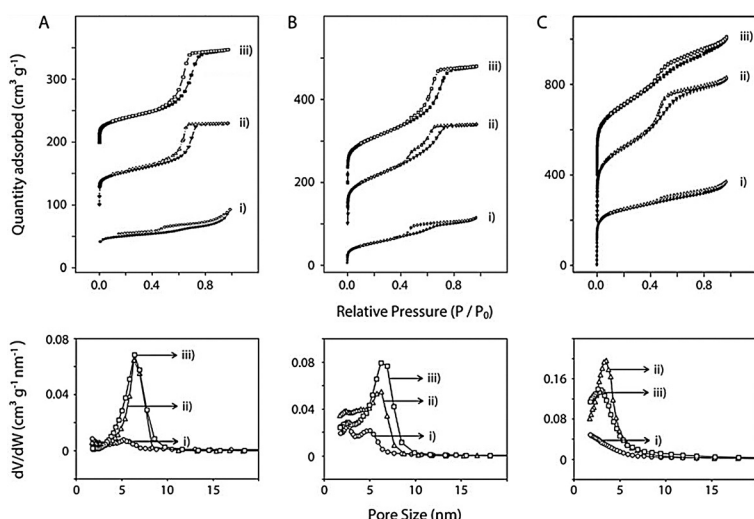
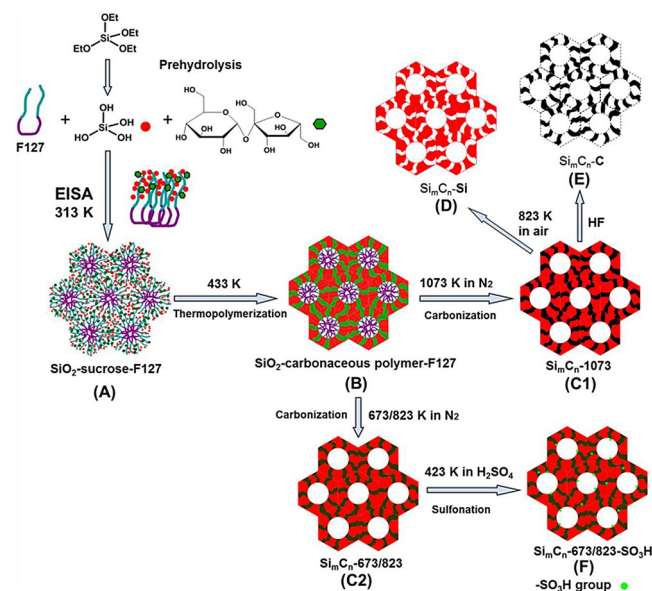


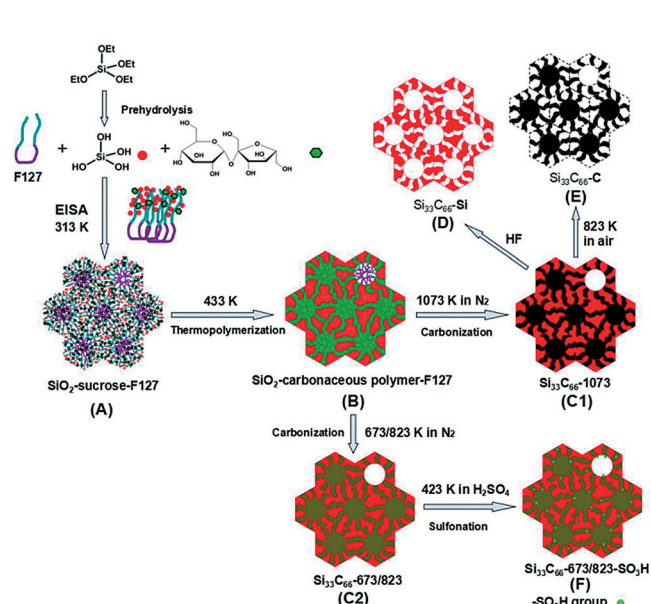
Figure 3. [Top] N₂ adsorption (closed symbols)/desorption (open symbols) isotherms and [Bottom] pore size distribution of A) composites, B) pure silica, and C) pure carbon materials derived from: i) Si₃₃C₆₆, ii) Si₅₀C₅₀, and iii) Si₆₆C₃₃. For clarity, the offset between the isotherms along the y-axis is 100 cm³ g⁻¹ in A/B and 200 cm³ g⁻¹ in C.



Scheme 1. Evaporation-induced triconstituent assembly (EISA) to ordered mesoporous silica-carbon composites, sulfonated mesoporous silica-carbon composites and the corresponding ordered mesoporous silica and porous carbon materials in the case of moderate to low C content (Si₅₀C₅₀ and Si₆₆C₃₃). Red represents silica, while green to black represents carbonaceous component.

and Si₆₆C₃₃ (F127/TEOS/sucrose = 1:1.3:0.44 in mass ratio), the excessive part of sucrose molecules can blend with the entire F127 copolymer and enter the hydrophobic polypropylene oxide (PPO) cores of the micelles (Scheme 2A). Sucrose acts together with F127 as structure-directing agent besides as the carbon precursor when its concentration is higher than a certain "saturation" value of embedding in the silica network in the pore-walls. Notably, pure mesoporous carbon cannot be obtained directly from the co-assembly of sucrose and F127 without the addition of silica source,^[38] probably resulting from

the severe penetrating of sucrose into the PPO cores of the copolymer F127 micelles, which destroys the ordered distribution of carbon species in the final product. However, pure silica mesostructure with 2D hexagonal *p6mm* symmetry can be obtained at the TEOS/F127 mass ratio ranging from 1 to 2 via similar EISA process.^[39] Therefore, in our synthesis, the mesostructural ordering increases with the increase of silica/carbon ratio and a too-high amount of sucrose causes a structural disordering, although the basic *p6mm* symmetry of the packing of the micelles is unchanged. This is quite different from the silica-carbon nanocomposites



Scheme 2. EISA to silica-carbon nanocomposite of high C content (Si₃₃C₆₆), the corresponding ordered mesoporous silica and porous carbon materials, and its derived sulfonated silica-carbon composites. Red represents silica, while green to black represents carbonaceous component.

prepared from the phenolic resin-TEOS-F127 system. A hexagonal mesostructure without silica component can be obtained directly from the assembly of phenolic resin around F127 micelles.^[29,31] In that case, the mass ratio of silica/phenolic resin can be tuned arbitrarily without collapsing the mesostructure.

The SiO₂-Sucrose-F127 composite was thermopolymerized at 433 K to produce SiO₂-carbonaceous polymer-F127 (Scheme 1B) and further pyrolyzed to produce Si_mC_n-T (Scheme 1C1 and 1C2). The transformation of the carbon and silica species during these processes was monitored by ¹³C CP-MAS and ²⁹Si solid-state MAS NMR respectively and the results

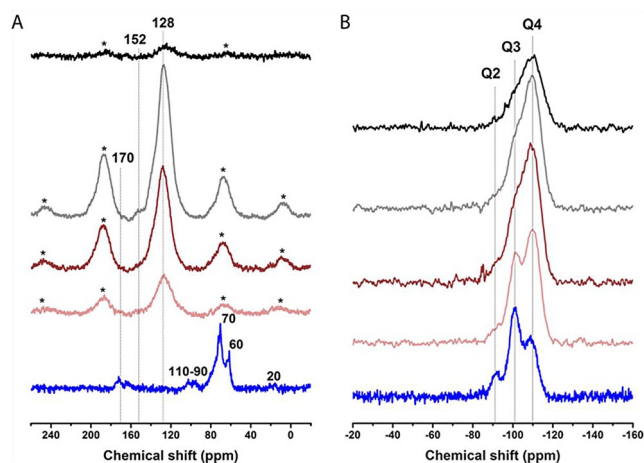


Figure 4. A) ^{13}C and B) ^{29}Si CP-MAS NMR spectra of (blue) $\text{Si}_{66}\text{C}_{33}$, (light red) $\text{Si}_{50}\text{C}_{50}$ -673- SO_3H , (dark red) $\text{Si}_{50}\text{C}_{50}$ -823- SO_3H , (grey) $\text{Si}_{50}\text{C}_{50}$ -823, and (black) $\text{Si}_{50}\text{C}_{50}$ -1073.

are shown in Figure 4. In the ^{13}C NMR spectrum of the as-synthesized $\text{Si}_{66}\text{C}_{33}$ (Figure 4A), peaks at ≈ 170 ppm and in the range of 110–90 ppm, which represents COOH groups and C=C of aromatics respectively, indicate that sucrose is primarily polymerized at 433 K. Carbonaceous polymers may be formed from sucrose by its dehydration into furan-like derivatives and further condensation with the hydroxymethylene CH_2OH groups. The C–O groups in such humin-like chemical structures should correspond to the broad ^{13}C NMR peak in the range of 90–55 ppm. Notably, there are two distinctively sharp peaks, at 70 and 60 ppm respectively, overlapping with the broad peak. They are ascribed to CH–O and CH_2 –O groups of F127 respectively, together with the peak at ≈ 20 ppm, which represents aliphatic carbon, confirming the presence of F127 in the as-synthesized nanocomposites. The sharp signal from ether structures of F127 in contrast with the broad signal from those of sucrose-derived saccharoidal-like polymers, implies a higher mobility of the carbon of F127, which strongly supports the proposed image that F127 forms relatively independent hexagonally-arranged arrays but sucrose is closely entangled in the silica framework in the stage of EISA.

In the ^{13}C NMR spectra of $\text{Si}_{50}\text{C}_{50}$ after pyrolysis at 673, 823, or 1073 K (Figure 4A), the peak at ≈ 20 ppm for aliphatic carbon, as well as the sharp peaks in the range of 90–55 ppm disappeared, which indicates the removal of F127 template during pyrolysis at temperatures higher than or equal to 673 K. The desorption and decomposition of F127 would create porosity in the nanocomposites (Scheme 1C1 and 1C2). Simultaneously, the broad peak for C–O in sucrose-derived polymers disappeared whereas the peak at 128 ppm became dominant. This peak is assigned to aromatic carbon, characteristic of carbon materials from pyrolysis.^[20,40] Indeed, sucrose molecules start to form polycyclic aromatic carbon sheets for pyrolysis temperatures above 573 K by further converting furan rings to benzene rings.^[32,41] Since sulfonation would not affect the ^{13}C NMR spectra as indicated by the very similar patterns of $\text{Si}_{50}\text{C}_{50}$ -823 and $\text{Si}_{50}\text{C}_{50}$ -823- SO_3H , the minor peaks at higher

chemical shifts, 170 and 152 ppm, besides the aromatic carbon peak of $\text{Si}_{50}\text{C}_{50}$ -673- SO_3H would result from the relatively low pyrolysis temperature applied. The peaks at 170 and 152 ppm are assigned to COOH groups and OH-substituted carbons of phenols respectively.^[20,40] The presence of oxygen-containing species in the carbon phase in the silica-carbon nanocomposites may impact the surface properties and in turn the catalytic performance. When the pyrolysis temperature was elevated to 823 K, the peak for polycyclic aromatic carbon grew stronger but the peaks for carbons binding with oxygen atoms became weaker, indicating the growth and aggregation of carbon sheets in the silica-carbon nanocomposites during pyrolysis in N_2 . By further raising the pyrolysis temperature to 1073 K, the oxygen-containing carbon species were eliminated with the exclusively one peak at 128 ppm left. Moreover, this peak decreased largely in intensity which probably results from a high graphitization degree in $\text{Si}_{50}\text{C}_{50}$ -1073.

The ^{29}Si solid-state MAS NMR spectra of silica-carbon nanocomposites before and after pyrolysis are shown in Figure 4B. Three peaks at -91 , -101 and -110 ppm, which correspond to Q2 ($\text{Si}(\text{OSi})_2(\text{OH})_2$), Q3 ($\text{Si}(\text{OSi})_3(\text{OH})$) and Q4 ($\text{Si}(\text{OSi})_4$) type of silica respectively, are observed in the ^{29}Si NMR spectrum of the as-synthesized $\text{Si}_{66}\text{C}_{33}$. After pyrolysis, Q2 and Q3 contents decreased significantly while Q4 content increased. With the increase of pyrolysis temperature, Q3/Q4 decreased to a larger extent. In the $\text{Si}_{50}\text{C}_{50}$ -1073, the Q2 and Q3 types of silica almost disappeared with only Q4 silica species left. These results indicate that during the pyrolysis, silica were continuously solidified by condensation and cross-linking. A rigid silica framework can be obtained by pyrolysis at a high temperature.

Furthermore, the ^{13}C CP-MAS and ^{29}Si solid-state MAS NMR spectra of these pyrolyzed silica-carbon nanocomposites show no indication of the formation of Si–C species (Figure 4). Hence, it is plausible that the structure of silica-carbon nanocomposite would be superposition of the structures of its derived pure silica and carbon materials by removal of carbon and silica component respectively. On account of the rigidity of the silica framework, pure silica materials Si_mC_n -Si (Scheme 1D and 2D) after the burn-off of carbon component show an unchanged mesostructure with newly generated ≈ 2.6 nm mesopores in addition to the primary ≈ 6.2 nm mesopores, compared to their parent silica-carbon nanocomposite Si_mC_n -1073. Nevertheless, pure carbon materials Si_mC_n -C (Scheme 1E) after etching of silica component show a deteriorated ordering of mesostructure with a large amount of small mesopores (< 4 nm). Hence, the parent silica-carbon nanocomposites possess a “homogeneous” framework constituted by nanosized silica and carbon components interpenetrated with each other. For $\text{Si}_{33}\text{C}_{66}$ where sucrose is in a too-high amount, the pyrolyzed material is microporous as most of the large mesopores are filled with amorphous carbon sheets from excessive sucrose penetrated into the PPO micell cores (Scheme 2C1 and 2C2).

Sulfonation of the mesostructured silica-carbon nanocomposites and their acid properties

To evaluate the catalytic potential of these novel mesoporous silica-carbon nanocomposites, the as-synthesized Si_mC_n nanocomposites were pyrolyzed at a moderate temperature (673 or 823 K) and functionalized with sulfonic acid groups. The unique characteristics of silica-carbon nanocomposites, due to the combination of well-ordered mesostructure of silica and easy functionalization of carbon component, are promising to fabricate such solid-acid catalysts with a high amount of easily accessible SO_3H groups. It is known that SO_3H can be introduced into the incompletely carbonized sugar by sulfonation with concentrated H_2SO_4 .^[32] Meanwhile, silica component serve as a rigid support to maintain the ordered mesostructure during the harsh sulfonation treatment.^[33,42]

The textural properties of these sulfonated silica-carbon nanocomposites were studied with SAXS and N_2 sorption measurements (Figure S3 and S4). The results are summarized in Table 1, entries 13–18. Sulfonation would hardly influence the pore structure, except for slight loss of carbonaceous species, owing to side-reactions such as oxidation and dehydration during sulfonation.^[42] Therefore, the textural parameters of Si_mC_n -673/823- SO_3H are similar to those of Si_mC_n -673/823, which differ from Si_mC_n -1073 merely by the lowering of the pyrolysis temperature. Since there is no severe degradation of mesostructure ordering even when pyrolysis was performed at 1073 K, the mesostructure of Si_mC_n -673/823- SO_3H sample would be more or less the same with the above-analyzed structure of Si_mC_n -1073. The SAXS patterns of Si_mC_n -673/823- SO_3H samples (Figure S3) all show a scattering peak, assigned to the (100) reflection of the hexagonal mesostructure. The calculated pore distance is consistent with the rule that slight shrinkage of the framework occurs during pyrolysis. Among samples pyrolyzed at the same temperature, the scattering peak of $\text{Si}_{33}\text{C}_{66}$ -673/823- SO_3H is the weakest and corresponding to a slightly larger pore distance than $\text{Si}_{50}\text{C}_{50}$ -673/823- SO_3H and $\text{Si}_{66}\text{C}_{33}$ -673/823- SO_3H . These results also imply that excessive sucrose in the synthesis of $\text{Si}_{33}\text{C}_{66}$ samples can penetrate into the hydrophobic domain of the F127 micelles and expand the pore structure, but impair the ordering of the mesostructure at the same time. The N_2 sorption isotherms of $\text{Si}_{50}\text{C}_{50}$ -673/823- SO_3H and $\text{Si}_{66}\text{C}_{33}$ -673/823- SO_3H samples (Figure S4A) show a typical type IV curve with a H1-type hysteresis loop. They are well-ordered cylindrical mesoporous materials, with a narrow pore size distribution centered at ≈ 7 nm (Figure S4B). On the contrary, $\text{Si}_{33}\text{C}_{66}$ -673- SO_3H is microporous and $\text{Si}_{33}\text{C}_{66}$ -823- SO_3H has no porous structure at all (Figure S4), as a result from the excess of carbon in the F127-derived mesopores. Notably, the samples pyrolyzed at 673 K all possess high micropore volume with respect to those pyrolyzed at higher temperatures, perhaps due to the loose packing and incomplete formation of carbon sheets at 673 K.

The acid properties of these sulfonated silica-carbon nanocomposites were investigated by FTIR and TMPO probed ^{31}P NMR spectroscopy. The FTIR spectra of Si_mC_n -673/823- SO_3H (Figure S5) show that with the increase of pyrolysis tempera-

ture, the intensity of the stretching vibration band of $\text{C}=\text{O}$ decreases, but the intensity of the stretching vibration band of $\text{C}=\text{C}$ increases, as a result of the increased carbonization degree. However, the stretching bands of SO_3H cannot be differentiated for the overlapping with the strong bands of $\text{Si}-\text{O}$ stretching. In the FTIR spectra of HF solution-treated Si_mC_n -823- SO_3H samples (Figure S6),[†] the bands at 1032 and 1007 cm^{-1} for the stretching of SO_3H groups are visible, showing the successful functionalization of these silica-carbon nanocomposites with SO_3H groups. The density of SO_3H groups was determined by titration and correlated with the carbon content of the sample as show in Figure S7. SO_3H site density increases linearly with the carbon content at the respective pyrolysis temperature, which indicates that similar carbonization degree of sucrose is obtained, thus showing similar reactivity towards H_2SO_4 . However, the slope of the fitting line for the pyrolysis temperature of 823 K is smaller than the one for 673 K, indicating that larger carbon sheets formed at higher pyrolysis temperature can be closely packed and with less oxygen-containing groups,^[40] and therefore more difficult to be sulfonated.

The ^{31}P NMR spectra obtained after an adequate amount of TMPO adsorption and evacuation on these sulfonated silica-carbon nanocomposites are shown in Figure 5. The dashed curves indicate Gaussian deconvolution of the spectra. The absence of resonance peaks at 41 ppm for all the ^{31}P NMR spectra indicates that no excess of TMPO aggregates on the surface and is a proof of sufficient evacuation.^[40,43] The resonance peaks can be divided into three categories. Peaks at 78–

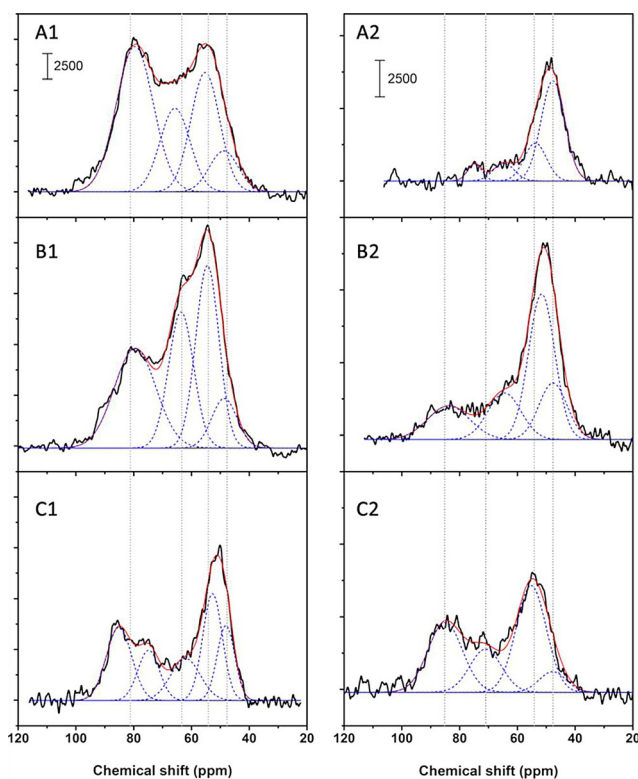


Figure 5. ^{31}P NMR spectra of catalysts after adsorption of trimethylphosphine oxide (TMPO): A1) $\text{Si}_{33}\text{C}_{66}$ -673- SO_3H , A2) $\text{Si}_{33}\text{C}_{66}$ -823- SO_3H , B1) $\text{Si}_{50}\text{C}_{50}$ -673- SO_3H , B2) $\text{Si}_{50}\text{C}_{50}$ -823- SO_3H , C1) $\text{Si}_{66}\text{C}_{33}$ -673- SO_3H , and C2) $\text{Si}_{66}\text{C}_{33}$ -823- SO_3H .

86 ppm are ascribed to TMPO adsorbed on strong acid sites, i.e., SO_3H groups in these sulfonated materials, in consistency with the previous assignments of TMPO-probed ^{31}P MAS NMR spectra of sulfonated carbon.^[20,40] Peaks at lower chemical shifts, ≈ 75 , 65, 54 ppm can be assigned to TMPO adsorbed on weak acid sites like COOH, phenolic OH and Si–OH. Peaks at 48 ppm are ascribed to physisorbed TMPO. For samples pyrolyzed at 673 K (Figure 5A1, 5B1, and 5C1), similar high chemical shifts for TMPO on SO_3H groups are observed, which indicates that similar acid strength is obtained after sulfonation of the carbonaceous phase. The areal percentage of this peak in the total ^{31}P resonance peaks decreases from 43 to 32 to 25% for $\text{Si}_{33}\text{C}_{66}$ -673- SO_3H , $\text{Si}_{50}\text{C}_{50}$ -673- SO_3H , and $\text{Si}_{66}\text{C}_{33}$ -673- SO_3H . These results are in line with the SO_3H group densities determined by titration. However, an opposite trend to the results of titration is found for the ^{31}P resonance peak areas, corresponding to SO_3H groups on the 823 K-pyrolyzed samples (Figure 5A2, 5B2, and 5C2). The area percentage of this peak increases from 0 to 17 to 32% with the decrease of carbon content, whereas the titration data showed a decrease of acidity with decreasing carbon content. This phenomenon is likely due to significant structural restriction around the strong acid sites on these 823 K-pyrolyzed samples. By referring to the textural properties of these sulfonated silica-carbon composites (Table 1, entries 13–18), the decreased mesoporous ordering with the increased carbon content in the pore structure is regarded as the major cause of a reduced accessibility of TMPO molecules to the SO_3H groups.

Performance in acid catalysis

The catalytic performance of sulfonated silica-carbon nanocomposites was demonstrated through dimerization of styrene and dimerization of α -methylstyrene. The reaction scheme of dimerization of styrene is shown in Scheme S1. Protonated styrene reacts with another styrene monomer to form a dimeric carbocation intermediate which either deprotonates into a head-to-tail dimer 1,3-diphenyl-1-butene (DPB) or into 1-methyl-3-phenylindan (MPI) by intramolecular Friedel–Crafts alkylation which requires relatively strong acid sites.^[44] Small amounts of trimers and adducts with toluene (the solvent) were also detected as side products.

The time courses of styrene conversion and the selectivities of DPB and MPI are shown in Figure 6. The reactivity of styrene over these catalysts follows the order of Nafion NR-50 > $\text{Si}_{66}\text{C}_{33}$ -673- SO_3H > $\text{Si}_{66}\text{C}_{33}$ -823- SO_3H > $\text{Si}_{50}\text{C}_{50}$ -673- SO_3H > CBV720 > $\text{Si}_{50}\text{C}_{50}$ -823- SO_3H > $\text{Si}_{33}\text{C}_{66}$ -673- SO_3H . In contrast, $\text{Si}_{33}\text{C}_{66}$ -823- SO_3H , Sugar-673- SO_3H , and Sugar-823- SO_3H show almost no conversion even after 24 h, indicating the diffusion limitations of styrene molecules to sulfonic acid groups in these non-porous structures. These internal sulfonic acid sites in $\text{Si}_{33}\text{C}_{66}$ -823- SO_3H have been demonstrated not accessible with TMPO molecules, see Figure 5A2. Considering the larger dynamic diameter of styrene compared to TMPO, it is reasonable to assume that styrene cannot access the carbon sheets of the carbon phase in the composite $\text{Si}_{33}\text{C}_{66}$ -823- SO_3H . It is similarly understandable that $\text{Si}_{33}\text{C}_{66}$ -673- SO_3H shows a rather low reac-

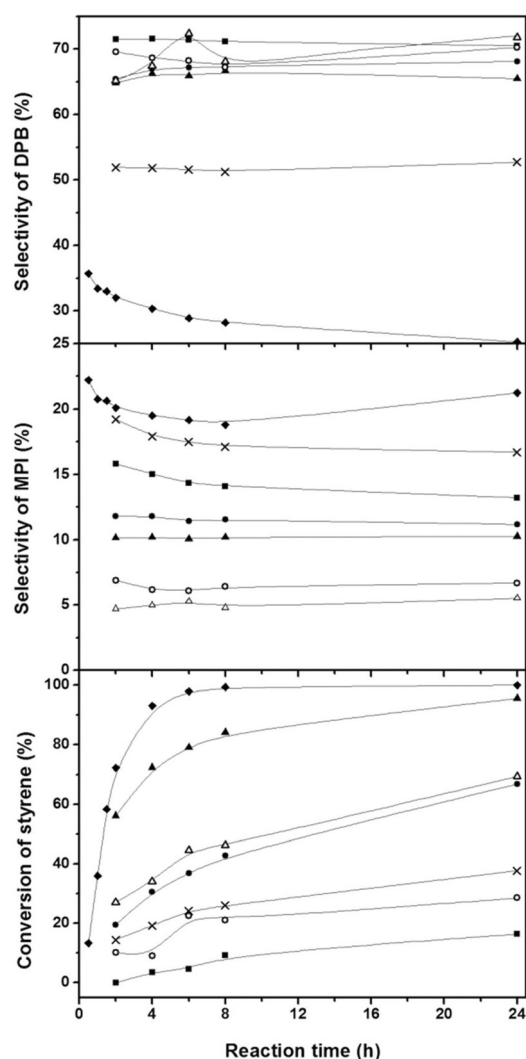


Figure 6. Dimerization of styrene over sulfonated silica-carbon nanocomposites. (■) $\text{Si}_{33}\text{C}_{66}$ -673- SO_3H , (●) $\text{Si}_{50}\text{C}_{50}$ -673- SO_3H , (▲) $\text{Si}_{66}\text{C}_{33}$ -673- SO_3H , (○) $\text{Si}_{50}\text{C}_{50}$ -823- SO_3H , (△) $\text{Si}_{66}\text{C}_{33}$ -823- SO_3H , (×) CBV720, and (◆) Nafion NR50. Reaction conditions: styrene (0.50 g), catalyst (50 mg), toluene (5.00 g), reaction temperature 373 K.

tivity for styrene, despite it bears a high amount of SO_3H sites in micropores which are accessible to TMPO molecules (Figure 5A1). Hence, accessible (effective) sulfonic acid groups to styrene molecules are entailed for the dimerization of styrene.

Nafion NR50 shows the highest activity of styrene conversion. However, the selectivity towards the linear unsaturated dimer, DPB, is much lower than all the sulfonated silica-carbon nanocomposites and higher amounts of cyclic indanic dimer, MPI and adducts of styrene with toluene were produced. Such relatively low selectivity of DPB is also observed with CBV720. It is very possible that the Brønsted acidities of Nafion NR50 and CBV720 are so strong that not only catalyze the equilibrium reaction of the protonated dimer intermediate to DPB, but also catalyze the intramolecular and intermolecular electrophilic substitution reactions. In comparison, the selectivities of DPB over sulfonated silica-carbon nanocomposites were remarkably high, between 65 to 72% during the reaction course, and the

Table 2. Dimerization of styrene and AMS by sulfonated silica-carbon nanocomposite catalysts.

	[SO ₃ H] ^[a] [mmol g ⁻¹]	Rate of DPB ^[b] [μmol h ⁻¹]	TOF of DPB ^[c] [h ⁻¹]	Rate of unsaturated dimers from AMS ^[d] [μmol h ⁻¹]	TOF of unsaturated dimers from AMS ^[e] [h ⁻¹]
Si ₃₃ C ₆₆ -673-SO ₃ H	0.57	15.1	0.5	412.2	14.5
Si ₅₀ C ₅₀ -673-SO ₃ H	0.40	153.3	7.7	935.2	46.8
Si ₆₆ C ₃₃ -673-SO ₃ H	0.31	436.2	28.1	1867.5	120.5
Si ₃₃ C ₆₆ -823-SO ₃ H	0.37	trace	trace	n.d.	n.d.
Si ₅₀ C ₅₀ -823-SO ₃ H	0.25	84.7	4.6	n.d.	n.d.
Si ₆₆ C ₃₃ -823-SO ₃ H	0.15	211.8	28.2	n.d.	n.d.
CBV720 ^[f]	0.56	89.7	3.2	6351.1	226.8
Nafion NR50	0.80	228.2	5.7	33.6	0.8

[a] The density of SO₃H group was determined from titration. [b] The formation rate of DPB was calculated from the early stage of dimerization of styrene. [c] TOF of DPB was calculated from the formation rate of DPB normalized to per acid site. [d] The formation rate of unsaturated dimers was calculated from the early stage of dimerization of AMS. [e] TOF of unsaturated dimers from AMS was calculated from the formation rate of unsaturated dimers normalized to per acid site. [f] Acid sites in CBV720 was H⁺.

selectivities for MPI were all below 15%. It is largely due to the moderate Brønsted acidity of sulfonic acid groups bound to polycyclic aromatic carbon in these sulfonated silica-carbon nanocomposites. Furthermore, the coexistence of phenolic OH groups in thus pyrolyzed carbon may also account for the restriction of intramolecular Friedel–Crafts alkylation, as suggested recently by others.^[45] Among all these catalysts tested, the highest activity towards the formation of DPB was obtained over Si₆₆C₃₃-673-SO₃H (The selectivity of DPB reached 66% at the conversion of 96% after 24 h), see the plots of the selectivity of DPB versus conversion of styrene in Figure S8.

The formation rate of DPB, calculated from the early stage of dimerization of styrene and the TOF (turnover frequency), calculated from the formation rate normalized to per acid site, are listed in Table 2. Of the silica-carbon nanocomposites pyrolyzed at the same temperature, the formation rate and TOF of DPB both increase with the decrease of carbon content in the nanocomposite. The nanocomposite of a lower carbon content possesses a lower SO₃H site density but shows a significantly higher TOF of DPB, supporting that this reaction is controlled by diffusion of styrene molecules to the SO₃H sites in the carbon domains in the nanocomposites. Seeing the physicochemical properties of sulfonated silica-carbon nanocomposites in Table 1, entries 13–18, mesoporosity, rather than surface area and total porosity, is found to nicely correlate with the TOFs of DPB over these nanocomposites. For Si₃₃C₆₆-673-SO₃H with little mesoporosity, dimerization of styrene can only slowly proceed. For Si₅₀C₅₀-673/823-SO₃H and Si₆₆C₃₃-673/823-SO₃H where sulfonated carbon sheets are well incorporated in the silica-supported pore walls with ≈7 nm mesopores open, dimerization of styrene into DPB can be facilitated. Comparing nanocomposites of the same starting silica-carbon ratio but pyrolyzed at different temperatures, the TOFs of DPB are quite comparable, due to the similar mesostructure and thus similar spatial constraints for the dimerization of styrene. In addition, the selectivities of MPI in the 823 K-pyrolyzed nanocomposites are lower than their 673 K-pyrolyzed counterparts, probably arising from the lower density of SO₃H groups.

The dimerization of α-methyl styrene (AMS) was also performed in the presence of these sulfonated silica-carbon nanocomposites. The reaction Scheme of the dimerization of AMS is shown in Scheme S2. Three dimerization products, unsaturated acyclic dimers (2,4-diphenyl-4-methyl-1-pentene (1-DPMP) and 2,4-diphenyl-4-methyl-2-pentene (2-DPMP)) and a saturated dimer (1,1,3-trimethyl-3-phenylindane (TMPI)) were detected. The time courses of the conversion of AMS, the selectivities of unsaturated dimers and saturated TMPI are shown in Figure 7. The selectivities for the

unsaturated dimers (1-DPMP and 2-DPMP) are close to 100% over the Si_mC_n-673-SO₃H catalysts, whereas over CBV720 and Nafion NR50, side product TMPI is produced in a much larger quantity. These results indicate that the acid strength SO₃H groups in the sulfonated silica-carbon nanocomposites can protonate the C=C double bond of AMS for dimerization, but not that strong for a Friedel–Crafts alkylation to the indane dimer of AMS. The initial formation rates of unsaturated dimers from AMS and the TOFs are listed in Table 2. Similar activity order to the dimerization of styrene is observed for the dimerization of AMS over the Si_mC_n-673-SO₃H catalysts. With the increase of silica-carbon ratio, the formation rate of unsaturated dimers of AMS increases and the TOF increases more conspicuously, showing the crucial effect of large mesoporosity for the dimerization of AMS. The structural contribution of silica component in these mesostructures ensures such accessible SO₃H groups for AMS molecules.

Conclusions

We have demonstrated that a broad family of silica-carbon materials can be synthesized by an EISA approach from the system of sucrose-TEOS-F127 and the latter removal of carbon or silica component, as shown in Scheme 3. By changing the initial amount of sucrose, the pore structure of the silica-carbon nanocomposites can be tuned while the silica part keeps a 2D hexagonal mesoporous framework. A possible mechanism of the formation of the silica-carbon composites was proposed and analyzed with the combination of the results of SAXS, TEM, N₂ sorption, and NMR. It is found that silica-carbon composites after pyrolysis are mesoporous and composed of homogeneously interpenetrating silica and carbon components; while they lose mesoporosity when F127-derived mesopores are occupied by the excessive carbonized sucrose as in the case of Si₃₃C₆₆. Such series of silica-carbon composites pyrolyzed at moderate temperatures were functionalized with SO₃H groups and can act as efficient and selective acid catalysts in the dimerization of styrene to DPB and di-

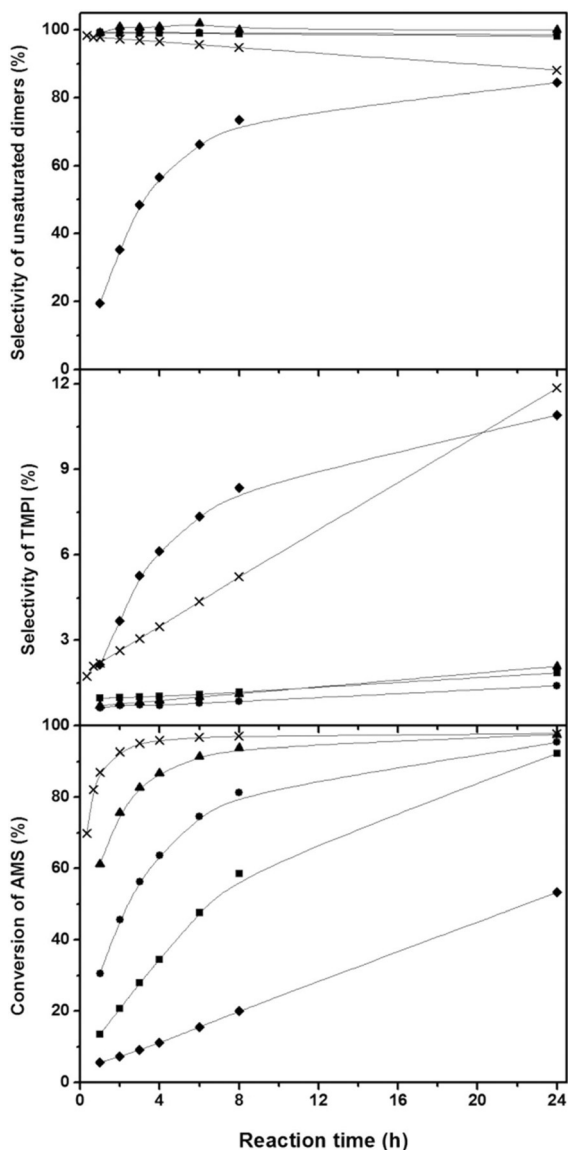
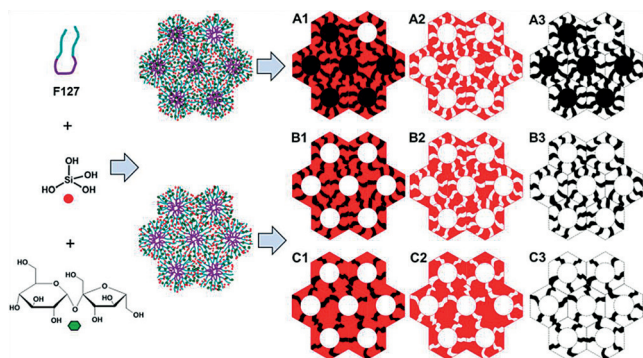


Figure 7. Dimerization of AMS over (■) $\text{Si}_{33}\text{C}_{66}$ -673- SO_3H , (●) $\text{Si}_{50}\text{C}_{50}$ -673- SO_3H , (▲) $\text{Si}_{66}\text{C}_{33}$ -673- SO_3H , (×) CBV720, and (◆) Nafion NR50. Reaction conditions: AMS (0.73 g), catalyst (50 mg), toluene (5.22 g), reaction temperature 323 K.



Scheme 3. Summary of materials derived in this study by applying EISA synthesis of F127, TEOS and sucrose. A, B, and C represent $\text{Si}_{33}\text{C}_{66}$, $\text{Si}_{50}\text{C}_{50}$, and $\text{Si}_{66}\text{C}_{33}$, respectively.

merization of α -methylstyrene to unsaturated dimers. Acidity was carefully analyzed with titration, FTIR and TMPO-probed ^{31}P NMR to offer a clear understanding of these dimerization reactions.

Experimental Section

Synthesis of ordered mesoporous silica-carbon composites

Mesoporous silica-carbon composites were synthesized by the evaporation-induced triconstituent assembly method, wherein sucrose was used as carbon precursor, prehydrolyzed TEOS as silica precursor, and triblock copolymer F127 as template (Scheme 1).^[35] Three samples with different carbon content were synthesized. In a typical synthesis, 6.4 g of block copolymer F127 (Pluronic F127, $\text{EO}_{106}\text{PO}_{70}\text{EO}_{106}$, $M_w = 12600$) was dissolved in ethanol (32 g) with concentrated HCl (37%, 0.3 g) and the mixture was treated in an ultrasonic bath for 1 h to afford a clear solution. In parallel, sucrose (5.7 g) was dissolved in deionized water (10 g). Then, the sucrose solution and 8.32 g of TEOS were added into the mixture. The mixture was sonicated for another 1 h to form a homogeneous solution. The solution was transferred into dishes to evaporate ethanol at 313 K during 20 h following by heating treatment at 433 K for 24 h to thermopolymerize sucrose. The as-made product, named as $\text{Si}_{50}\text{C}_{50}$, was scraped from the dishes. The composites with a different initial carbon content of 66 wt% and 33 wt%, denoted as $\text{Si}_{33}\text{C}_{66}$ and $\text{Si}_{66}\text{C}_{33}$ respectively, were prepared according to a similar procedure of $\text{Si}_{50}\text{C}_{50}$ by varying the mass ratios of sucrose to TEOS. Pyrolysis was performed in a tubular furnace at 673 or 823 K for 15 h or at 1073 K for 2 h under N_2 flow to remove the F127 template and further carbonize sucrose. The pyrolyzed silica-carbon composites were denoted as $\text{Si}_m\text{C}_n\text{-}T$, where m and n represent the initial weight percentages of silica and carbon components and T represents the pyrolysis temperature in Kelvin.

Synthesis of silica and carbon materials from silica-carbon composites

The pyrolyzed nanocomposites, Si_mC_n -1073, were calcined at 823 K for 5 h in air to burn off carbon to obtain the pure mesoporous silica samples, Si_mC_n -Si. The nanocomposite was also immersed in a 10 wt% HF solution (20 mL per gram of sample) at room temperature for 24 h. The black solid was washed repeatedly with H_2O until F^- was not detected with CaCl_2 . The resultant product was named Si_mC_n -C, corresponding to its parent nanocomposite.

Preparation of sulfonic acid group-functionalized mesoporous silica-carbon composite

Nanocomposites pyrolyzed at moderate temperatures, Si_mC_n - T (T equals 673 or 823 K), were treated with concentrated sulfuric acid (20 mL per gram of sample) in Teflon-lined autoclaves at 423 K for 15 h. The solid was washed extensively with hot distilled water (>353 K) until no sulfate ions were detected with $\text{Ba}(\text{NO}_3)_2$. The product was named Si_mC_n - T - SO_3H according to its parent nanocomposite.

Characterization

The SAXS patterns were recorded at the Dutch–Belgian beamline (BM26) of the European Synchrotron Radiation Facility and a custom software was used to reduce the measured 2D data into

1D scattering patterns.^[46] Average distance between neighboring pores was calculated as $4\pi/\sqrt{3}q^*$, where q^* is the scattering vector of the first peak. Nitrogen sorption isotherms were measured with a Micromeritics Tristar 3000 apparatus at 77 K. Prior to measurements, samples were pretreated at 393 K for 10 h in a N₂ flow. The Brunauer–Emmett–Teller surface area (S_{BET}) was calculated over a relative pressure range of 0.05 to 0.30. The total pore volume (V_{tot}) was calculated from the saturation plateau of adsorption at high relative pressures. Mesopore volume (V_{meso}) was calculated after subtraction of the micropore volume (V_{micro}) as obtained by the t-plot method. Average mesopore diameter (D) was calculated from the adsorption branch of the isotherms, based on the Brunauer–Joyner–Halenda (BJH) method. Transmission electron microscopy (TEM) images were acquired on a Philips CM30 microscope operated at 300 kV. Samples were dispersed in ethanol by sonication and deposited onto a holey-carbon-film support grid. Thermogravimetric analyses (TGA) were performed on a Q500 equipment (TA Instruments, Brussels, Belgium). Weight losses were monitored as the samples were heated from room temperature to 1073 K at 5 K min⁻¹ under O₂. ¹³C CP-MAS NMR spectra were collected using a Bruker DSX400 spectrometer ($B_0=9.4$ T) at room temperature with a frequency of 100.61 MHz, a recycle delay of 10 s and a contact time of 5.0 ms. The sample was packed in a 4 mm zirconia rotor and the spinning frequency was 6 kHz. Tetramethylsilane was used as a chemical shift reference. The extremely long relaxation delay of carbon materials made it infeasible to conduct single-pulse measurements for quantitative determinations. Thus, the CP/MAS spectra of ¹³C were applied to qualitative comparisons among samples, assuming similar cross-polarization capabilities of the ¹³C resonance signals. ²⁹Si solid-state MAS NMR spectra were collected using a Bruker AMX300 spectrometer ($B_0=7.0$ T) at room temperature with a frequency of 59.63 MHz and a recycling delay of 60 s. The sample was packed in a 4 mm zirconia rotor and the spinning frequency was 5 kHz. Tetramethylsilane was also used as a reference material. The Brønsted acid strength and content of the sulfonated silica-carbon nanocomposites was examined by ³¹P MAS NMR. The sample was first evacuated at 423 K for 2 h and immersed in a tetrahydrofuran (THF) solution which contained an adequate amount of trimethylphosphine oxide (TMPO) for 20 h. After evacuation of removing the THF solvent, the sample was packed in a 4 mm zirconia rotor in a N₂ glovebox. ³¹P NMR spectra were collected on a Bruker AMX300 spectrometer ($B_0=7.0$ T) with a recycle delay of 60 s and a rotor spinning frequency of 6 kHz. An aqueous solution of orthophosphoric acid (85%) was used as a chemical shift reference.

Catalytic reaction

Acid catalysis of the sulfonated silica-carbon nanocomposites were demonstrated by dimerization of styrene and α -methyl styrene (AMS). For comparison, an ion-exchanged resin (Nafion NR50), a zeolite (CBV720) and sulfonated sugar catalysts prepared from direct pyrolysis of sucrose (Sugar-673-SO₃H and Sugar-823-SO₃H)^[32] were also tested under the same reaction conditions. Prior to reactions, all catalysts were dehydrated at 423 K overnight. Dimerization of styrene was performed in a closed glass vial. Styrene (0.50 g) was reacted over the catalyst (50 mg) in toluene (5.00 g, solvent) at 373 K in the presence of *n*-decane (0.73 g, internal standard) under magnetic stirring. Samples were withdrawn at regular intervals from the reaction mixtures and analyzed by a GC-FID instrument using a capillary column. Similarly dimerization of α -methyl styrene was also conducted in a closed glass vial with AMS (0.73 g) and *n*-decane (0.73 g, internal standard) in toluene (5.22 g)

in the presence of the solid catalyst (50 mg) at 323 K. Samples were withdrawn at intervals and analyzed by GC.

Acknowledgements

The authors thank the long-term structural funding of the Flemish government (Methusalem). They are also grateful to the Belgian Science Policy (Belspo) for providing financial support (FdC) and to the KU Leuven (OT 11/061). RZ thanks the China Scholarship Council (No. 201206210307) financial support. We are grateful to Kristof Houthoofd for his support in the NMR analysis.

Keywords: acid catalysis • dimerization of styrene • heterogeneous catalysis • porous carbon • silica-carbon nanocomposite

- [1] F. de Clippel, M. Dusselier, S. Van de Vyver, L. Peng, P. A. Jacobs, B. F. Sels, *Green Chem.* **2013**, *15*, 1398–1430.
- [2] D. E. De Vos, M. Dams, B. F. Sels, P. A. Jacobs, *Chem. Rev.* **2002**, *102*, 3615–3640.
- [3] A. Taguchi, F. Schuth, *Microporous Mesoporous Mater.* **2005**, *77*, 1–45.
- [4] M. Hartmann, *Chem. Mater.* **2005**, *17*, 4577–4593.
- [5] Z. Wu, D. Zhao, *Chem. Commun.* **2011**, *47*, 3332–3338.
- [6] B. J. Scott, G. Wirnsberger, G. D. Stucky, *Chem. Mater.* **2001**, *13*, 3140–3150.
- [7] M. Manzano, M. Vallet-Regi, *J. Mater. Chem.* **2010**, *20*, 5593–5604.
- [8] F. Schüth, *Chem. Mater.* **2001**, *13*, 3184–3195.
- [9] S. Polarz, M. Antonietti, *Chem. Commun.* **2002**, 2593–2604.
- [10] Y. Wan, H. Yang, D. Zhao, *Acc. Chem. Res.* **2006**, *39*, 423–432.
- [11] C. Liang, Z. Li, S. Dai, *Angew. Chem. Int. Ed.* **2008**, *47*, 3696–3717; *Angew. Chem.* **2008**, *120*, 3754–3776.
- [12] J. Shi, Z. Hua, L. Zhang, *J. Mater. Chem.* **2004**, *14*, 795–806.
- [13] M. L. Anderson, R. M. Stroud, D. R. Rolison, *Nano Lett.* **2002**, *2*, 235–240.
- [14] M. Choi, F. Kleitz, D. Liu, H. Y. Lee, W. S. Ahn, R. Ryoo, *J. Am. Chem. Soc.* **2005**, *127*, 1924–1932.
- [15] F. de Clippel, A. Harkiolakis, X. Ke, T. Vosch, G. Van Tendeloo, G. Baron, P. Jacobs, J. Denayer, B. Sels, *Chem. Commun.* **2010**, *46*, 928–930.
- [16] F. de Clippel, A. Harkiolakis, T. Vosch, X. Ke, L. Giebeler, S. Oswald, K. Houthoofd, J. Jammaer, G. Van Tendeloo, J. Martens, P. Jacobs, G. Baron, B. Sels, J. Denayer, *Microporous Mesoporous Mater.* **2011**, *144*, 120–133.
- [17] H. Kim, J. Cho, *Nano Lett.* **2008**, *8*, 3688–3691.
- [18] T. Kwon, H. Nishihara, Y. Fukura, K. Inde, N. Setoyama, Y. Fukushima, T. Kyotani, *Microporous Mesoporous Mater.* **2010**, *132*, 421–427.
- [19] H. Nishihara, Y. Fukura, K. Inde, K. Tsuji, M. Takeuchi, T. Kyotani, *Carbon* **2008**, *46*, 48–53.
- [20] K. Nakajima, M. Okamura, J. N. Kondo, K. Domen, T. Tatsumi, S. Hayashi, M. Hara, *Chem. Mater.* **2009**, *21*, 186–193.
- [21] Y. Wan, H. Wang, Q. Zhao, M. Klingstedt, O. Terasaki, D. Zhao, *J. Am. Chem. Soc.* **2009**, *131*, 4541–4550.
- [22] M. Tsionsky, G. Gun, V. Glezer, O. Lev, *Anal. Chem.* **1994**, *66*, 1747–1753.
- [23] Y. Mastai, S. Polarz, M. Antonietti, *Adv. Funct. Mater.* **2002**, *12*, 197–202.
- [24] J. Pang, V. T. John, D. A. Loy, Z. Yang, Y. Lu, *Adv. Mater.* **2005**, *17*, 704–707.
- [25] B. Toury, F. Babonneau, *J. Eur. Ceram. Soc.* **2005**, *25*, 265–270.
- [26] Z. Yang, Y. Xia, R. Mokaya, *J. Mater. Chem.* **2006**, *16*, 3417–3425.
- [27] P. Valle-Vigón, M. Sevilla, A. B. Fuertes, *Microporous Mesoporous Mater.* **2010**, *134*, 165–174.
- [28] S. S. Park, Y. Jung, C. Xue, R. Che, D. Zhao, C. Ha, *Chem. Mater.* **2010**, *22*, 18–26.
- [29] R. Liu, Y. Shi, Y. Wan, Y. Meng, F. Zhang, D. Gu, Z. Chen, B. Tu, D. Zhao, *J. Am. Chem. Soc.* **2006**, *128*, 11652–11662.
- [30] Q. Hu, R. Kou, J. Pang, T. L. Ward, M. Cai, Z. Yang, Y. Lu, J. Tang, *Chem. Commun.* **2007**, 601–603.
- [31] Y. Meng, D. Gu, F. Zhang, Y. Shi, L. Cheng, D. Feng, Z. Wu, Z. Chen, Y. Wan, A. Stein, D. Zhao, *Chem. Mater.* **2006**, *18*, 4447–4464.

- [32] M. Toda, A. Takagaki, M. Okamura, J. N. Kondo, S. Hayashi, K. Domen, M. Hara, *Nature* **2005**, *438*, 178–178.
- [33] L. Peng, A. Philippaerts, X. Ke, J. Van Noyen, F. De Clippel, G. Van Tendeloo, P. A. Jacobs, B. F. Sels, *Catal. Today* **2010**, *150*, 140–146.
- [34] M. Kruk, M. Jaroniec, R. Ryoo, S. H. Joo, *J. Phys. Chem. B* **2000**, *104*, 7960–7968.
- [35] S. Van de Vyver, L. Peng, J. Geboers, H. Schepers, F. De Clippel, C. Gommès, B. Goderis, P. A. Jacobs, B. F. Sels, *Green Chem.* **2010**, *12*, 1560–1563.
- [36] S. Schlienger, A. Graff, A. Celzard, J. Parmentier, *Green Chem.* **2012**, *14*, 313–316.
- [37] Y. Wei, J. Xu, H. Dong, J. H. Dong, K. Qiu, S. A. Jansen-Varnum, *Chem. Mater.* **1999**, *11*, 2023–2029.
- [38] A reference sample derived from the co-assembly of F127 and sucrose without the addition of silica source was prepared and its N₂ sorption analysis results show no mesoporosity.
- [39] W. Chu, S. Chiang, J. Li, S. Kuo, *RSC Adv.* **2014**, *4*, 784–793.
- [40] M. Okamura, A. Takagaki, M. Toda, J. N. Kondo, K. Domen, T. Tatsumi, M. Hara, S. Hayashi, *Chem. Mater.* **2006**, *18*, 3039–3045.
- [41] R. J. White, V. Budarin, R. Luque, J. H. Clark, D. J. Macquarrie, *Chem. Soc. Rev.* **2009**, *38*, 3401–3418.
- [42] P. Valle-Vigón, M. Sevilla, A. B. Fuertes, *Appl. Surf. Sci.* **2012**, *261*, 574–583.
- [43] F. de Clippel, M. Dusselier, R. Van Rompaey, P. Vanelderen, J. Dijkmans, E. Makshina, L. Giebeler, S. Oswald, G. V. Baron, J. F. M. Denayer, P. P. Pescarmona, P. A. Jacobs, B. F. Sels, *J. Am. Chem. Soc.* **2012**, *134*, 10089–10101.
- [44] A. Corma, H. Garcia, *J. Chem. Soc. Dalton Trans.* **2000**, 1381–1394.
- [45] S. Suganuma, K. Nakajima, M. Kitano, H. Kato, A. Tamura, H. Kondo, S. Yanagawa, S. Hayashi, M. Hara, *Microporous Mesoporous Mater.* **2011**, *143*, 443–450.
- [46] C. J. Gommès, B. Goderis, *J. Appl. Crystallogr.* **2010**, *43*, 352–355.

Received: June 25, 2015

Published online on September 3, 2015